Progress in Natural Science: Materials International 30 (2020) 393–401

HOSTED BY

Contents lists available at ScienceDirect

Progress in Natural Science: Materials International

journal homepage: www.elsevier.com/locate/pnsmi

Original Research

Structure and corrosion resistance of Al–Cu–Fe alloys

Rafał Babilas[a,*], Anna Bajorek[b], Monika Spilka[a], Adrian Radoń[c], Wojciech Łoński[a]

[a] Department of Engineering Materials and Biomaterials, Silesian University of Technology, Konarskiego 18a St., 44-100, Gliwice, Poland
[b] Institute of Physics, University of Silesia in Katowice, 75 Pułku Piechoty 1, 41-500 Chorzow, Poland
[c] Łukasiewicz Research Network - Institute of Non-Ferrous Metals, Sowińskiego 5 St., 44-100, Gliwice, Poland

ARTICLE INFO

Keywords:
Al-Cu-Fe alloys
Copper mold casting
X-ray diffraction
High-resolution transmission electron microscopy
X-ray photon spectroscopy
Electrochemical impedance spectroscopy

ABSTRACT

The microstructure and electrochemical properties of Al–Cu–Fe alloys with the atomic compositions of $Al_{65}Cu_{20}Fe_{15}$, $Al_{78}Cu_7Fe_{15}$ and $Al_{80}Cu_5Fe_{14}Si_1$ have been studied. The alloys were produced by induction melting of pure elements with copper mold casting. The microstructure of the alloys was analyzed by X-ray diffraction and high-resolution transmission electron microscopy. The formation of quasicrystalline phases in the Al–Cu–Fe alloys was confirmed. The presence of intermetallic phases was observed in the alloys after crystallization in a form of ingots and plates. The electrochemical measurements were conducted in 3.5% NaCl solution. The electronic structure of the alloys was determined by X-ray photoelectron spectroscopy. The post corrosion surface of the samples was checked using a scanning electron microscope equipped with the energy-dispersive X-ray detector. It was observed that the $Al_{65}Cu_{20}Fe_{15}$ alloy had the highest corrosion resistance. The improved corrosion resistance parameters were noted for the plate samples rather than those in the as-cast state. And the hardness of the $Al_{65}Cu_{20}Fe_{15}$ alloy was significantly higher than the other alloy samples.

1. Introduction

Aluminum alloys are one of the most important engineering materials. As we can noted in the works of Markoli et al. [1] and Školáková et al. [2] Al-based alloys have found applications in wide-ranging areas, such as automotive and aerospace industries due to their lightweight and excellent mechanical properties. What is more, Zupanič et al. [3] and Schurack et al. [4] indicated that alloys with a dominant aluminum content coupled with transition metals forming intermetallic phases with a complex structure (termed aluminum quasicrystalline alloys) constitute a new class of materials with great potential for the applications. In the last few years, a number of studies have been carried out on formation, structure, and physical properties of the quasicrystalline alloys [5–7].

The most common method used to obtain quasicrystalline phases is melting followed by rapid quenching. Currently, the preparation of quasicrystalline materials is possible by many manufacturing techniques such as utilizing a high-temperature synthesis [8], powder metallurgy [9] and rapid solidification of melt [10].

Göğebakan et al. [11] reported that the metastable quasicrystalline phases mainly form during the rapid cooling from liquids in binary and ternary alloys, whereas stable quasicrystalline phases form in ternary alloys, in which the presence of a third alloying component plays a stabilizing role. Quasicrystals are often solids with quasiperiodic atomic structures and without any translation symmetry as well as rotation symmetry with 5-, 8-, 10- or 12- fold axes, which cannot be observed in crystalline materials [12,13].

Alloys containing quasicrystals, due to their complicated atomic structure, exhibit a novel combination of properties. Suárez et al. [14], Huttunen-Saarivirta et al. [15] and Lee et al. [16] highlighted that quasicrystalline alloys have many unique properties, such as, low electrical and thermal conductivity, high corrosion and oxidation resistance, low friction coefficients, high abrasion resistance, high tensile strength, favorable elastic modulus, hardness and brittleness at room temperature. These unique properties mean that the quasicrystals can be used as anti-adhesives materials, protective coatings or the reinforcements of composites [17].

Li et al. [18] and Lityńska-Dobrzyńska et al. [19] reported that the main advantages of Al–Cu–Fe quasicrystals are their nontoxicity, easy availability, low cost and the possibility of recycling materials. The Al–Cu–Fe quasicrystals have an icosahedral structure and can be obtained only in a narrow atomic composition: 20–28% Cu, 10–14% Fe, and 60–70% Al. For example, Li et al. [20] stated that the $Al_{65}Cu_{20}Fe_{15}$ alloy was stable thermodynamically and did not exhibit any phase transformations up to its melting temperature at 1135 K.

Moreover, the influence of a wide range of dopants (Ti, V, Cr, Mn,

* Corresponding author.
E-mail address: rafal.babilas@polsl.pl (R. Babilas).

https://doi.org/10.1016/j.pnsc.2020.06.002
Received 22 January 2020; Received in revised form 19 May 2020; Accepted 5 June 2020
Available online 08 July 2020

Co, Ni, Si, Ge, Zr, Nb) in the quasicrystalline Al–Cu–Fe alloy has been investigated by Lee et al. [21] and Zhang et al. [22]. It was found that silicon can exist in the atomic structure of the alloy, stabilizing the icosahedral phase and increasing the temperature range of the quasicrystalline phase. The Al–Cu–Fe quasicrystals exhibit the exceptional mechanical properties and show good hardness (up to 10 GPa) and Young's modulus (up to 200 GPa). The thermal conductivity of quasicrystalline phase, related with a thermal expansion coefficient is close to metals. Mil'man et al. [12] reports that Al–Cu–Fe alloys sintered at high pressure and temperatures above 600–700 °C present high plasticity.

Much attention was devoted to physical properties investigations of these alloys [23]. It was found that Al–Cu–Fe quasicrystals showed peculiar physical properties such as high electrical resistivity, diamagnetism and a pseudogap at the Fermi level [24]. Moreover, the magnetoresistance of quasicrystals is anomalously large at low temperatures. The study of $Al_{65}Cu_{20}Fe_{15}$ quasicrystalline ribbons exhibited paramagnetic spectra in the temperature range from 4 to 300 K [25]. The behavior of icosahedral Al–Cu–Fe quasicrystal phase determined by some important magnetic factors is crucial in some industrial sectors [26].

The Al–Cu–Fe quasicrystalline alloys demonstrate high corrosion resistance and good hydrogen storage for the use in catalytic reactions. The Al–Cu–Fe alloys, at low temperatures, have similar thermal properties to zirconia oxides, which are considered as excellent insulators [27]. Massiani et al. [28] reported that the corrosion resistance depends on the alloy composition. Therefore, Rüdiger et al. [29] stated that corrosion of quasicrystals and crystalline phases in Al–Cu–Fe alloys should be studied from the electrochemical properties of the components.

The results published by Huttunen-Saarivirta et al. [30] show that the composition and number of phases formed in Al–Cu–Fe alloys are very important factor for the corrosion resistance. Moreover, the studies conducted in sulphuric acidic with different concentrations indicated that the corrosion behavior of the Al–Cu–Fe quasicrystalline alloys was not influenced by the structure but the composition of the other phases [31].

The results published by Ryabtsev et al. [32] showed that the quasicrystalline $Al_{65}Cu_{20}Fe_{15}$ alloy after corrosion in 5% NaCl solution at 293 K exhibited pitting corrosion only after 4 days. Many pits appearing on surface were a result of Fe and Al dissolution. The free corrosion potential was −0.66 V. Sukhova et al. [33] reported that Al–Cu–Fe alloys with Si dopant ensured the deceleration of the anodic reaction and the corrosion processes. The Si addition exhibited a positive impact on the corrosion resistance of the quasicrystal Al–Cu–Fe alloy.

The aim of this work is to prepare alloys with a quasicrystalline phase and examine their structure as well as their electrochemical properties.

2. Materials and experimental

The alloys with atomic compositions (at.%) of $Al_{65}Cu_{20}Fe_{15}$, $Al_{78}Cu_7Fe_{15}$ and $Al_{80}Cu_5Fe_{14}Si_1$ were prepared in the form of master alloys and plates in a two-stage process. The first stage was the preparation of ingots by induction melting of pure elements in an argon atmosphere. After that, the ingots were re-melted using an induction furnace under a argon atmosphere and cast into copper mold chilled by water (with a cooling rate $\sim 10^3$ K/s) [34]. The cooling rate of the alloy in the ceramic crucible is much lower than that in the copper form. This is due to factors such as a larger amount of alloy, lower ratio of surface to volume (cylinder in relation to the plate), lower thermal conductivity of ceramics in relation to copper and the lack of additional water cooling.

The structure of the master alloys and plates was verified by using a Rigaku MiniFlex 600 X-ray diffractometer equipped with a copper Cu Kα anode (λ = 0.15406 nm). Moreover, the structure of the $Al_{65}Cu_{20}Fe_{15}$ plates was studied by a high-resolution transmission electron microscope S/TEM TITAN 80–300 FEI. Samples were fragmented using an agate mortar. Then, subjected to ultrasound scattering in water, a small amount of suspension was successively applied to copper mesh with a carbon membrane.

The electrochemical measurements completed on the master alloys and plates were provided in an Autolab 302 N potentiostat at room temperature in 3.5% NaCl solution. The corrosion behaviour was analyzed by measuring the open-circuit potential (E_{OCP}) and potentiodynamic polarization curves. The three-electrode cell equipped in working electrode, saturated calomel electrode (SCE) and platinum rod as the counter electrode was used. The corrosion potential (E_{corr}), corrosion current density (j_{corr}), and polarization resistance (R_p) were determined by the Tafel extrapolation reported in Ref. [35].

In addition, electrochemical impedance spectroscopy (EIS) of the master alloys and plates was detected at open-circuit potentials with a perturbing signal of 5 mV, over a frequency range 10^5–10^{-2} Hz.

The electronic structure of the $Al_{65}Cu_{20}Fe_{15}$, $Al_{78}Cu_7Fe_{15}$ and $Al_{80}Cu_5Fe_{14}Si_1$ plates was determined by X-ray photoelectron spectroscopy (XPS) using a Physical Electronics (PHI 5700/660) spectrometer working in ultra-high vacuum (10^{-9} Torr) conditions and monochromatic Al *K*α X-ray source (1486.6 eV). The samples were kept under vacuum (10^{-9} Torr) for 12 h. Afterwards, the survey spectra were measured with a pass energy of 187.85 eV. The core level lines were recorded with a pass energy of 23.5 eV and with a standard limit of resolution set as 0.1 eV. All spectra were determined relative to the C1s peak (BE, Binding Energy, 284.8 eV). The collected data was analyzed by using MultiPak 9.2 software, which is referenced to the NIST XPS database.

The microstructure of the master alloys and in the form of plates was analyzed using a Zeiss Axio Observer light microscope. The morphology of the plates after electrochemical tests in 3.5% NaCl solution was analyzed using a scanning electron microscope (SEM) Supra 35 Carl Zeiss equipped with energy-dispersive X-ray spectroscopy (EDS) EDAX. The hardness tests of the plates were carried out using a Vickers Future Tech FM-700 with a penetrator load of 300 gf in 15 s.

3. Results

3.1. Microstructure characterization

The X-ray diffraction patterns of $Al_{65}Cu_{20}Fe_{15}$, $Al_{78}Cu_7Fe_{15}$, and $Al_{80}Cu_5Fe_{14}Si_1$ alloys in the form of master alloys and the plates are presented in Fig. 1. According to Calvayrac et al. [36] the diffraction peaks of $Al_{65}Cu_{20}Fe_{15}$ samples are assigned to an icosahedral phase. The remaining phases were defined as intermetallic phases. The most numerous Al–Cu–Fe ones were Cu_3Al, Al_2Cu, $Al_{13}Fe_4$, Al_7Cu_2Fe, AlFe, Al_2Fe, Al_6Fe. Moreover, the results from the X-ray diffraction measurements confirmed a multiphase structure of the studied alloys.

The presence of an Al–Cu–Fe quasicrystalline phase was confirmed in the plate sample of $Al_{65}Cu_{20}Fe_{15}$ alloy by means of electron diffraction. Fig. 2 presents a bright-field image and selected area electron diffraction pattern of $Al_{65}Cu_{20}Fe_{15}$ alloy. This is evidenced by a 5-fold axis of symmetry on the diffraction images, which is characteristic of the quasicrystalline phases.

Fig. 3 shows the representative light microscope images of the master alloys and plates of $Al_{65}Cu_{20}Fe_{15}$, $Al_{78}Cu_7Fe_{15}$, and $Al_{80}Cu_5Fe_{14}Si_1$ alloys, respectively. The structure changed from fine equiaxed crystals to coarse dendrites. The main difference between the structure of master alloys (ingots) and plates was the fragmentation of the structure (Fig. 3d,e,f). Additionally, the shapes of crystalline phases are changed. The phases detected in images of the plates had a shape which consists of alternation of the arranged strands. Most likely, they were placed parallel to the direction of the rapid heat dissipation during solidification of the alloy.

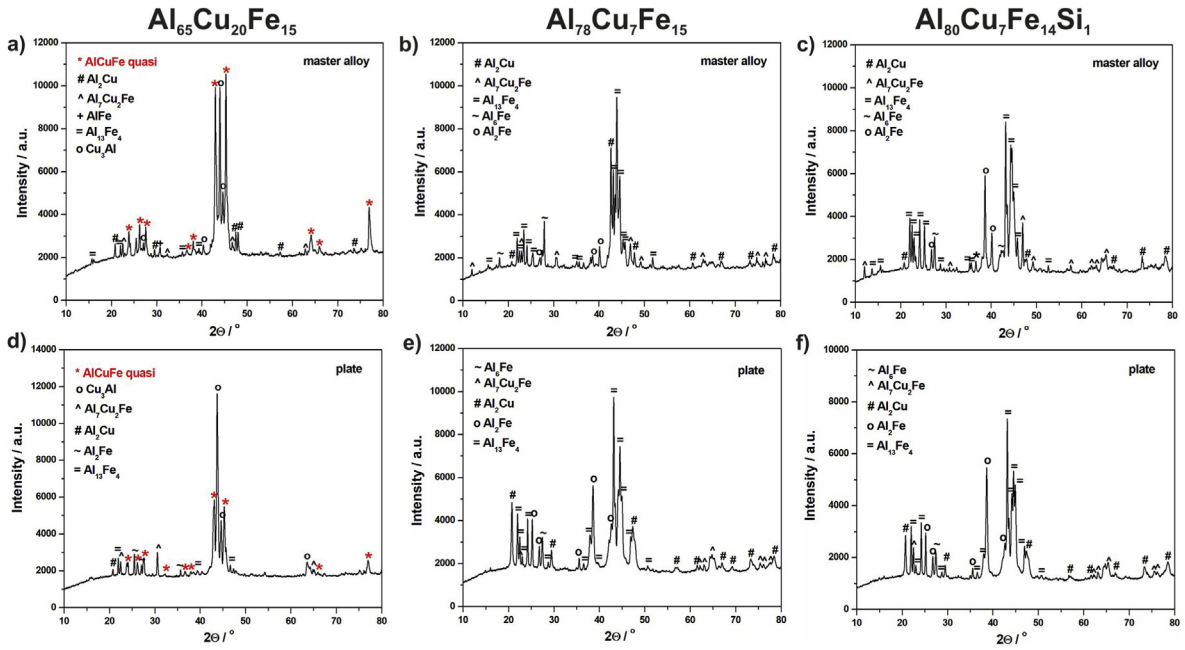

Fig. 1. XRD patterns of $Al_{65}Cu_{20}Fe_{15}$, $Al_{78}Cu_7Fe_{15}$, and $Al_{80}Cu_5Fe_{14}Si_1$ alloys in the form of master alloys (a,b,c) and plates (d,e,f).

3.2. Electrochemical measurements

The electrochemical tests of the master alloys and the plates were studied to determine their corrosion resistance in 3.5% NaCl solution. Moreover, open-circuit potential and potentiodynamic measurements were carried out at 25 °C (Fig. 4). The corrosion parameters including the open-circuit potential (E_{OCP}), corrosion current density (j_{corr}), corrosion potential (E_{corr}) and polarization resistance (R_p) are summarised

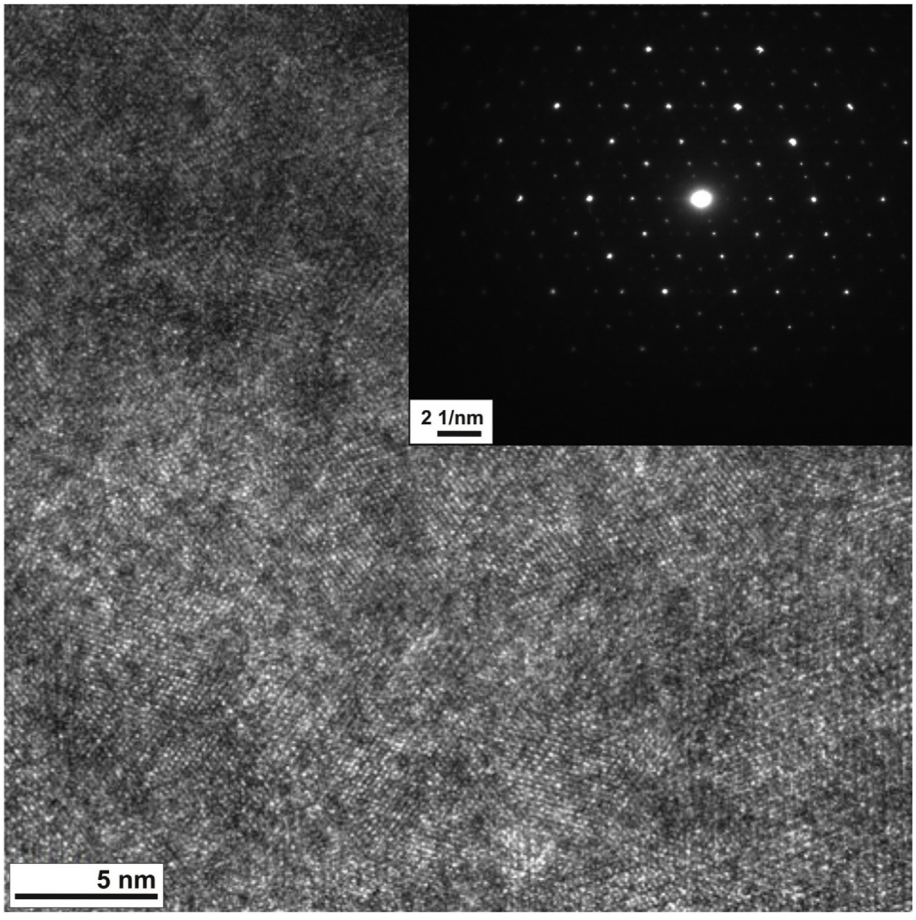

Fig. 2. HRTEM image and electron diffraction pattern of the $Al_{65}Cu_{20}Fe_{15}$ alloy in the form of the plate.

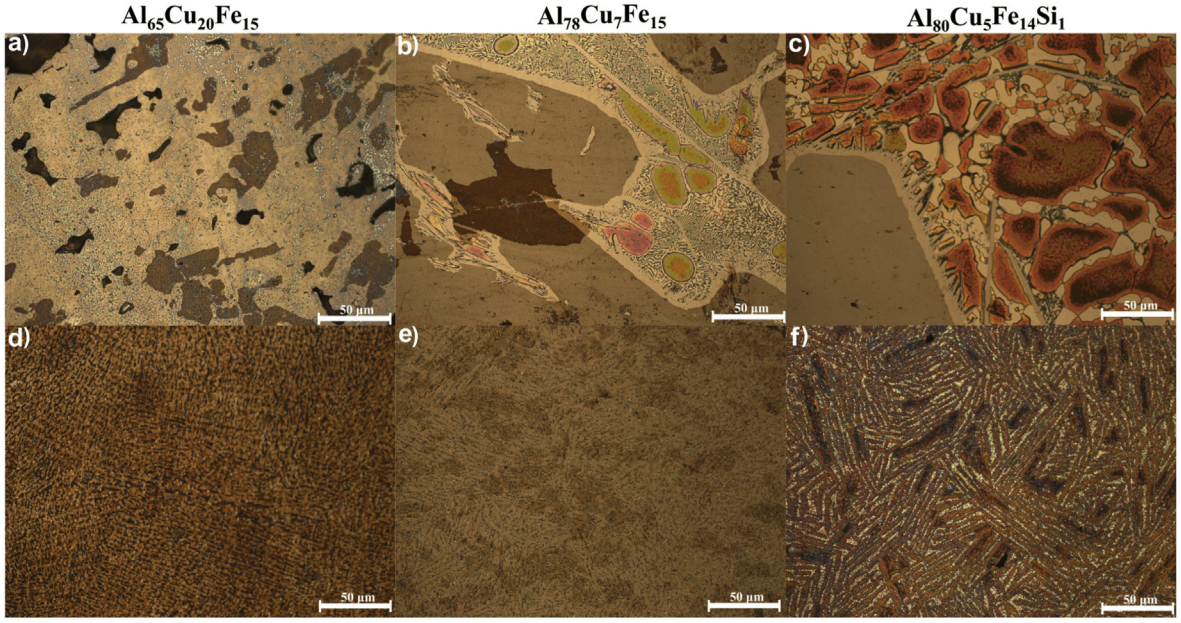

Fig. 3. LM images of $Al_{65}Cu_{20}Fe_{15}$, $Al_{78}Cu_7Fe_{15}$ and $Al_{80}Cu_5Fe_{14}Si_1$ alloys in the form of master alloys (a,b,c) and plates (d,e,f).

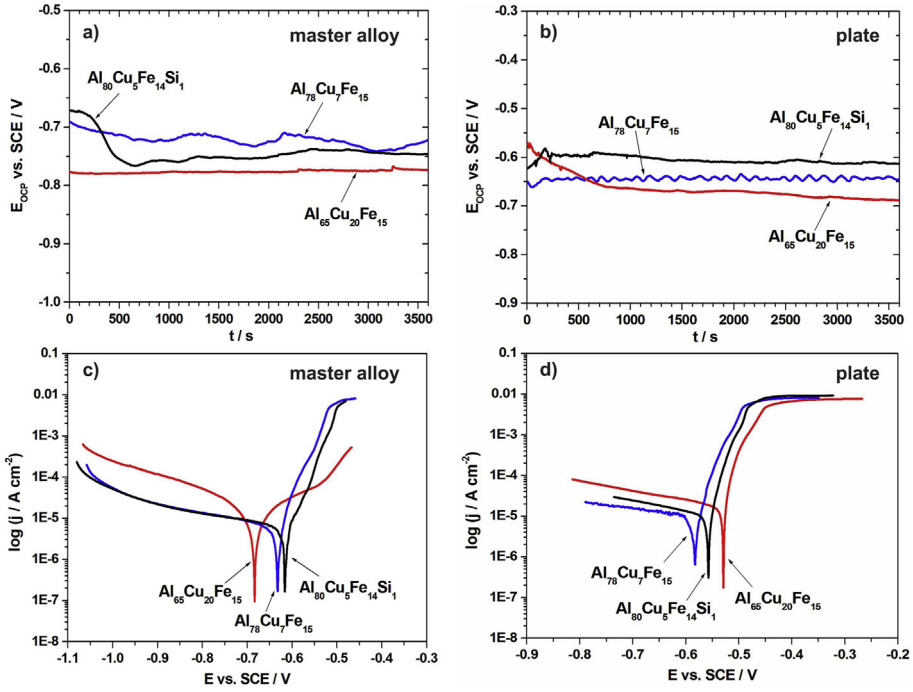

Fig. 4. Variation of the open-circuit potential with time (a,c) polarization curves and (b,d) in 3.5% NaCl solution, at 25 ˚C in the form of master alloys and plates.

Table 1
Results of the corrosion resistance of the $Al_{65}Cu_{20}Fe_{15}$, $Al_{78}Cu_7Fe_{15}$, $Al_{80}Cu_5Fe_{14}Si_1$ master alloys and plates in a 3.5% NaCl solution (E_{OCP} - open-circuit potential, E_{corr} - corrosion potential, R_p - polarization resistance, j_{corr} - corrosion current density).

Alloy	Form	E_{OCP} [V] (± 0.1)	E_{corr} [V] (± 0.1)	R_p [kΩcm^2] (± 0.1)	j_{corr} [μA/cm^2] (± 0.1)
$Al_{65}Cu_{20}Fe_{15}$	master alloy	−0.773	−0.683	2.43	37.1
	plate	−0.688	−0.529	0.42	14.3
$Al_{78}Cu_7Fe_{15}$	master alloy	−0.721	−0.631	2.52	5.6
	plate	−0.644	−0.582	1.71	1.6
$Al_{80}Cu_5Fe_{14}Si_1$	master alloy	−0.746	−0.615	2.45	13.7
	plate	−0.613	−0.557	1.24	2.1

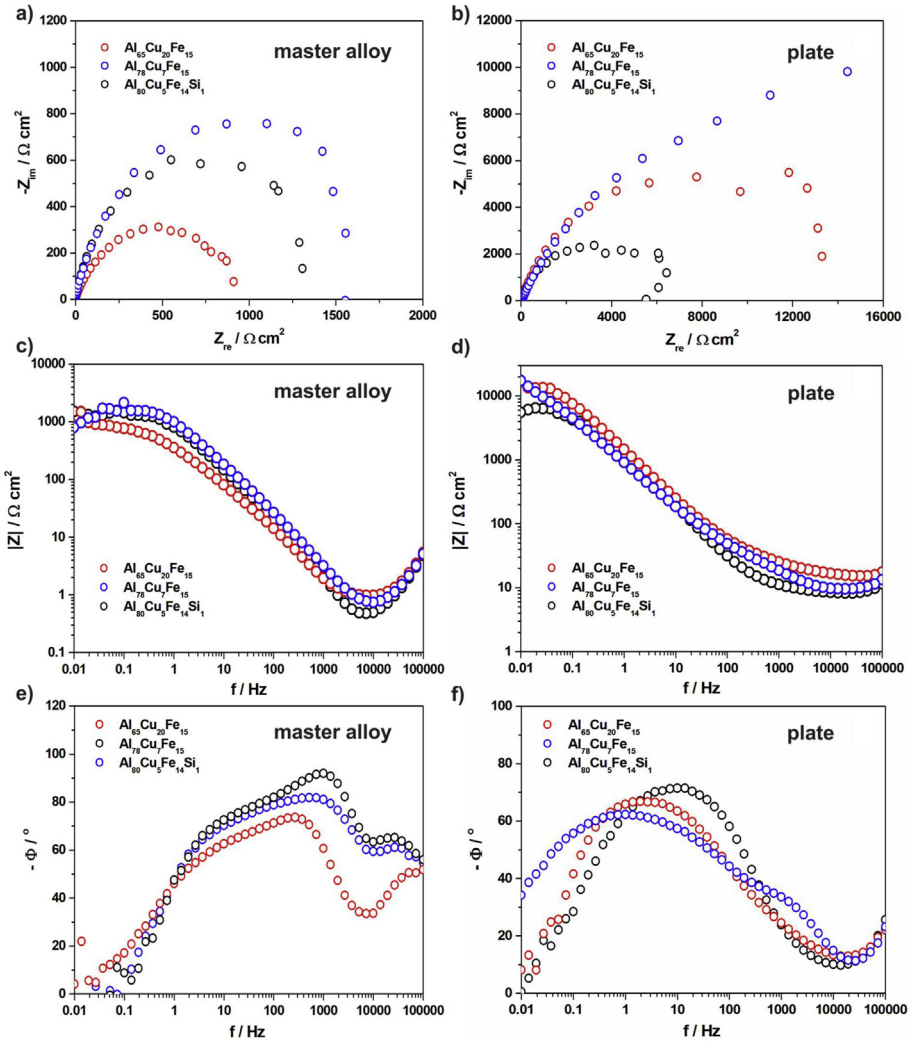

Fig. 5. Nyquist diagrams (a,b), Bode modulus diagrams (c,d) and Bode phase angle plots (e,f) in 3.5% NaCl solution at 25 °C for the selected samples in the form of master alloys and plates.

in Table 1.

During the recording of the E_{OCP}, in 3.5% NaCl solution, a decrease from −0.773 V ($Al_{65}Cu_{20}Fe_{15}$) to −0.721 V ($Al_{78}Cu_7Fe_{15}$) was noted for the master alloys (Fig. 4a). A similar decrease from −0.688 V ($Al_{65}Cu_{20}Fe_{15}$) to −0.613 V ($Al_{80}Cu_5Fe_{14}Si_1$) was observed for the plates (Fig. 4b). The $Al_{80}Cu_5Fe_{14}Si_1$ alloy, in the form of plate, gave an E_{OCP} value of −0.613 V and good stability.

Potentiodynamic studies of the alloys in 3.5% NaCl solution showed a drop of the corrosion potential for samples cast in the form of plates when compared with the master alloys. The E_{corr} value of the $Al_{65}Cu_{20}Fe_{15}$ master alloy was reduced from −0.683 V to −0.529 V for the as-cast state. Moreover, the lowest value of the corrosion potential was determined for the $Al_{65}Cu_{20}Fe_{15}$ alloy in the form of a plate. The other determined potentiodynamic parameters (j_{corr} and R_p) indicated also good corrosion resistance for the $Al_{78}Cu_7Fe_{15}$ alloy. The value of the corrosion current density and polarization resistance of the $Al_{78}Cu_7Fe_{15}$ plate was 1.6 μA/cm^2 and 1.71 kΩcm^2, respectively.

The EIS measurements were provided for alloys in 3.5% NaCl solutions at 25 °C to study the passivation behavior. The Nyquist and Bode diagrams of the master alloys and plates are presented in Fig. 5. The Nyquist plots manifested themselves as a single loop for each sample due to the resistance of the sample surface.

The Nyquist plots indicate that the diameter of the semicircle recorded for the $Al_{78}Cu_7Fe_{15}$ was higher compared to that of the $Al_{65}Cu_{20}Fe_{15}$ and $Al_{80}Cu_5Fe_{14}Si_1$ in a form of master alloys and plates, consequently (Fig. 5a and b). Moreover, the Nyquist plots confirm the increase in the corrosion resistance after rapid quenching conditions during pressure mold casting (Fig. 5b). This suggests that rapid cooling of the molten alloy improved the resistance when compared to the master alloy. The Bode-modulus plots indicate that the impedance is located over the range from 10^3 Ωcm^2 to 10^4 Ωcm^2 at low frequencies for the master alloys and plates, respectively (Fig. 5c and d). The phase angle increases from approximately −45° (for master alloys) to −65° (for samples cast in the form of plates) at a frequency of 1 Hz (Fig. 5e and f).

The EIS results were fitted to obtain an equivalent electric circuit included the ohmic resistance of the solution (R_s), the constant phase element (CPE) and the charge transfer resistance (R_t). The equivalent circuit demonstrates a presence of a layer of corrosion products upon the surface of the alloy and a charge transfer process. The results of fitting for the electric circuit components of the studied samples are listed in Table 2.

3.3. XPS study

Fig. 6 a,b,c represents the survey spectra after the corrosion measurements in 3.5% NaCl solution, for three studied plates with the nominal compositions of $Al_{65}Cu_{20}Fe_{15}$, $Al_{78}Cu_7Fe_{15}$, $Al_{80}Cu_5Fe_{14}Si_1$.

Table 2
Estimated values of the equivalent electric circuits of the $Al_{65}Cu_{20}Fe_{15}$, $Al_{78}Cu_7Fe_{15}$ and $Al_{80}Cu_5Fe_{14}Si_1$ master alloys and plates in a 3.5% NaCl solution (R_s - solution resistance, R_t - charge transfer resistance, *CPE* - constant phase element, *n* - empirical exponent).

Alloy	Form	R_s [kΩcm^2] (± 0.1)	R_t [kΩcm^2] (± 0.1)	*CPE* [μFcm^2] (± 0.1)	*n*
$Al_{65}Cu_{20}Fe_{15}$	master alloy	0.9	0.001	452.3	0.995
	plate	14.4	14.2	138.9	0.996
$Al_{78}Cu_7Fe_{15}$	master alloy	1.9	0.002	6469.6	0.998
	plate	26.9	26.3	604.4	0.995
$Al_{80}Cu_5Fe_{14}Si_1$	master alloy	0.001	1.5	153.0	0.998
	plate	9.2	6.3	10.4	0.997

The presented spectra were represented the elemental composition on the surface. Similarly, the survey spectra were collected after the last run of the sputtering procedure.

The characteristic photoemission main lines (C1s, O1s, Al2p, Cu2p, Fe2p and Si2p) and Auger peaks (O KLL, C KLL, Zn LMM, Mg KLL) correspond to the individual elements. Each of the studied specimens reveals the presence of less than 3 at.% impurities e.g.: Na1s, Cl2p, S2p, Si2p, and Ca2p, which were removed during the etching procedure by an Ar^+ beam. The first two impurities were a trace of NaCl solution.

The core level lines spectra for $Al_{65}Cu_{20}Fe_{15}$ are depicted in Fig. 7. The Al2p line at the surface (BE ≈ 73.7eV) is typical of Al_2O_3 states (stated by Ponja et al. [37]). During ion etching, this line is overlapped with Cu3p ($Cu3p_{3/2}$ - BE ≈ 75.6eV, $Cu3p_{1/2}$ - BE ≈ 77.8eV). Additionally, the emergence of pure Al2p states (BE ≈ 72.7 ± 0.5eV) is observed.

The Cu2p line at the surface is very low but not negligible and its weak intensity may be assigned to Cu_2S states located around 932.2 and 952.2 eV for $Cu2p_{3/2}$ and $Cu2p_{1/2}$, respectively. The first cleaning run using an argon beam leads to exposure typical CuO states with binding energies 933.8 and 953.6 eV for $Cu2p_{3/2}$ and $Cu2p_{1/2}$ lines, respectively, giving an L-S splitting of ΔE = 19.8 eV.

The Fe2p line with low intensity at the surface ($Fe3p_{3/2}$ - BE ≈ 710 eV and $Fe3p_{1/2}$ - BE ≈ 725 eV) is typical for Fe_2O_3 states. Just after the first cleaning runs using the argon beam, the double structure related to mixed Fe_2O_3 – pure Fe states were visible. Thus, by subsequent use of Ar^+ the pure Fe 2p line ($Fe3p_{3/2}$ - BE ≈ 706.4 eV and $Fe3p_{1/2}$ - BE ≈ 719.5 eV) with spin-orbit splitting of ΔE = 31.1 eV was observed.

The presence of Na1s and Cl2p lines was only on the surface. However, the presence of the Ca2p line waspuzzling. For two first alloys such impurity was noticeable at the surface, but for the $Al_{80}Cu_5Fe_{14}Si_1$ sample its presence was visible after 250 min of sputtering.

The surface dominant contaminant is carbon. The C1s line is composed of two peaks. The peak with the highest intensity represents the C - surface component (BE ≈ 284.8 eV), which was drastically reduced during ion etching. The second C - based peak with lower intensity (BE ≈ 288.6 eV), also reduced by the Ar^+ beam, is assigned to various carbonates.

The O1s core level line can be related by $Al(OH)_3$ (BE ≈ 531.4 eV) overlapped with $CuCO_3$ (BE ≈ 531.5 eV) compounds. Its further modification (line broadening and decreasing of its intensity) was related to the presence of various oxides and their change under the influence of the argon beam. After 250 min of sputtering the intensity of the O1s line was very small.

3.4. Surface morphology after corrosion

The SEM observations of samples after electrochemical tests revealed the slow corrosion and pitting corrosion of the $Al_{78}Cu_7Fe_{15}$ (Fig. 8e,f,g) and $Al_{80}Cu_5Fe_{14}Si_1$ (Fig. 8i,j,k) alloys. Subsequent observations using a scanning electron microscope also confirmed the pitting nature of corrosion in the $Al_{65}Cu_{20}Fe_{15}$ (Fig. 8a,b,c) alloy. The EDS (Fig. 8d,h,l) analysis was used to complement the XPS analysis and confirm the formation of aluminum hydroxides ($Al(OH)_3$) and iron oxides (Fe_2O_3). Sodium and chlorine on the surface of the samples were also detected. The results originate from the NaCl solution used in the corrosion tests. Aggregations of the corrosion products with extended morphology and corrosion centers were observed.

3.5. Hardness measurements

The highest value of the hardness was achieved for the $Al_{65}Cu_{20}Fe_{15}$ plate (Table 3). The hardness of the $Al_{78}Cu_7Fe_{15}$ and $Al_{80}Cu_5Fe_1Si_1$ alloys showed values of 495 and 468 HV, respectively. The highest hardness determined for the $Al_{65}Cu_{20}Fe_{15}$ (870 HV) alloy can be assumed to be a result of the occurrence of the quasicrystalline phase.

4. Discussion

The XRD analysis achieved by Huttunen-Saarivirtaa and Vuorinen [8] shows that the $Al_{65}Cu_{20}Fe_{15}$ alloy exhibits a multiphase structure with icosahedral $Al_{65}Cu_{20}Fe_{15}$ phases, cubic AlFe phases, monoclinic $Al_{13}Fe_4$ phases, and tetragonal Al_2Cu phase. Similarly to data described in Ref. [8] single-phase icosahedral ribbons prepared by the melt-spinning were not obtained. The ribbons exhibit a microstructure consisting three phases: the major icosahedral $Al_{65}Cu_{20}Fe_{15}$ phase, the minor cubic AlFe phase, and the monoclinic $Al_{13}Fe_4$ phase. In this work, the melt-spun ribbons show a three-phase structure composed of an icosahedral $Al_{65}Cu_{20}Fe_{15}$ phase, cubic AlFe and Cu_3Al phase.

Huttunen-Saarivirta et al. [30] indicated that for the $Al_{65}Cu_{20}Fe_{15}$ alloy, in 3.5% NaCl solution, the corrosion potential is −740 mV. The current density of the studied alloy reached a value of 6×10^{-1} μAcm^{-2}. The results indicate that amount of the phases formed in Al–Cu–Fe alloys are the key parameters for determining the corrosion behavior of this material. The corrosion potentials, determined in saline solutions, informed about homogeneous dissolution of the alloy followed by redeposition of Cu. The corrosion activity is determined by a volume of Cu-rich phases formed. What is more, Sukhova et al. [33] reported that Al–Cu–Fe alloys corrode in the sodium chloride solution. SEM results show the areas of pitting corrosion on the surface of investigated alloys. The pits appear mostly where iron-rich phases and phase interfaces are located. The corrosion resistance increased with a decrease in the iron-rich phase content in the doped alloys. This indicates the removal of oxide layers. The results were confirmed by microscopic observations. The number of pits was significantly higher than for the $Al_{65}Cu_{20}Fe_{15}$ alloy.

Sukhovaya et al. [38] reported the influence of silicon showing a decrease in the chemical activity of Al–Cu–Fe alloys. The most negative value of the stationary potential was determined for the non-doped $Al_{63}Cu_{25}Fe_{12}$ alloy. The values of the stationary potentials shift towards the more positive values as the Si addition increases. The positive influence of Si on the corrosion resistance of the Al–Cu–Fe alloys was confirmed by the investigations of the alloy surface exposed to saline solutions.

Hardness tests, used to verify the impact of composition on changes in the mechanical properties, showed that the highest hardness value was for the $Al_{65}Cu_{20}Fe_{15}$ alloy (870 HV). Suárez et al. [14] reported values of the hardness for each phase in the $Al_{65}Cu_{20}Fe_{15}$ alloy. The

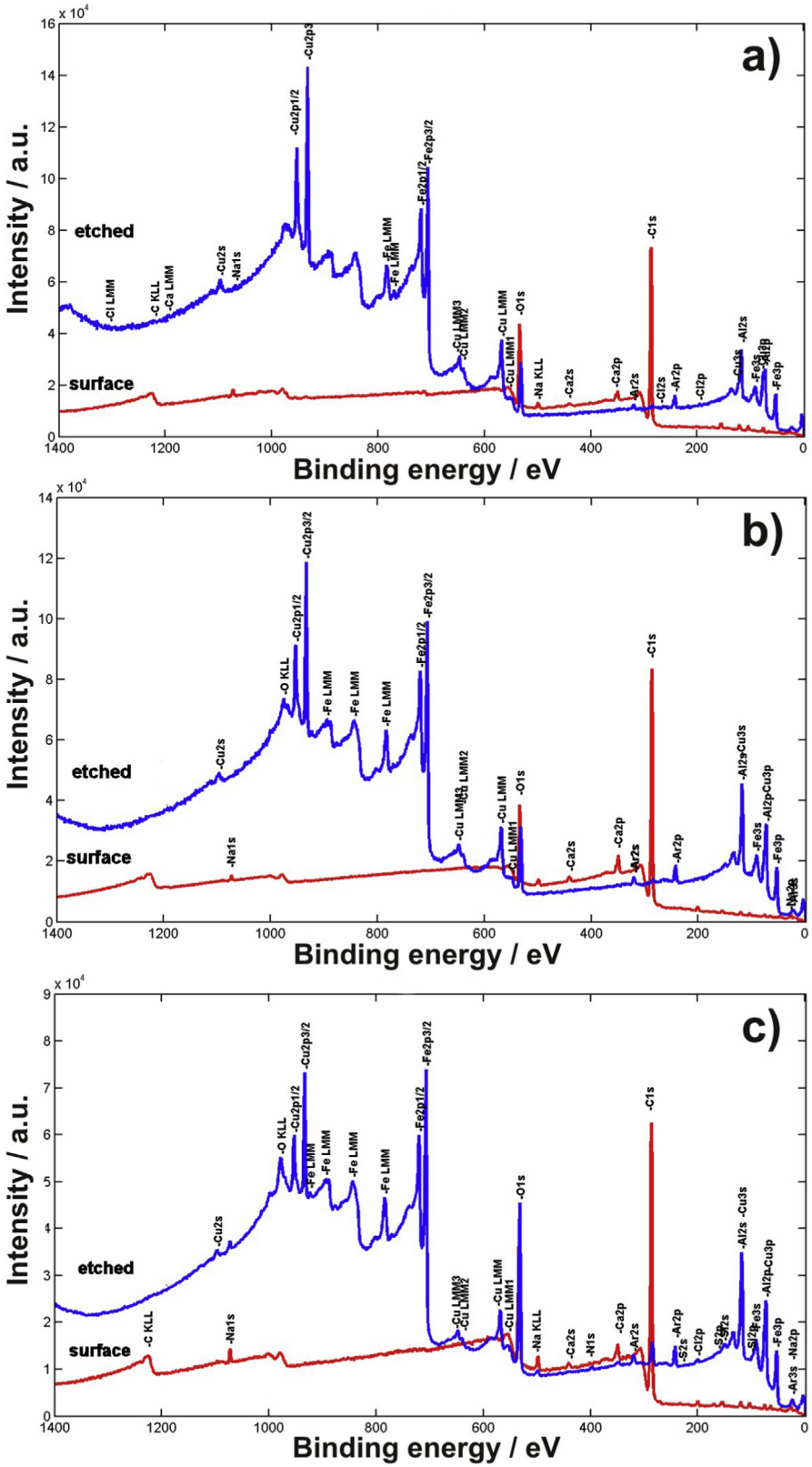

Fig. 6. XPS survey spectra, both before and after etching of $Al_{65}Cu_{20}Fe_{15}$ (a), $Al_{78}Cu_7Fe_{15}$ (b) and $Al_{80}Cu_5Fe_{14}Si_1$ (c) alloys after corrosion test in 3.5% NaCl solution at 25 °C.

highest hardness was reported in the monoclinic $Al_{13}Fe_4$ phase with a value of 758 HV, however, after heat treatment, the hardness of 844 HV was obtained for the icosahedral phase.

Lee et al. [21] presented the effect of Si addition into the $Al_{65}Cu_{20}Fe_{15}$ alloy on the change in hardness values. The highest value of hardness was observed for the $Al_{65}Cu_{20}Fe_{15}$ alloy (719 HV). The addition of silicon reduced the hardness to 596 HV for the $Al_{65}Cu_{20}Fe_{10}Si_5$ alloy.

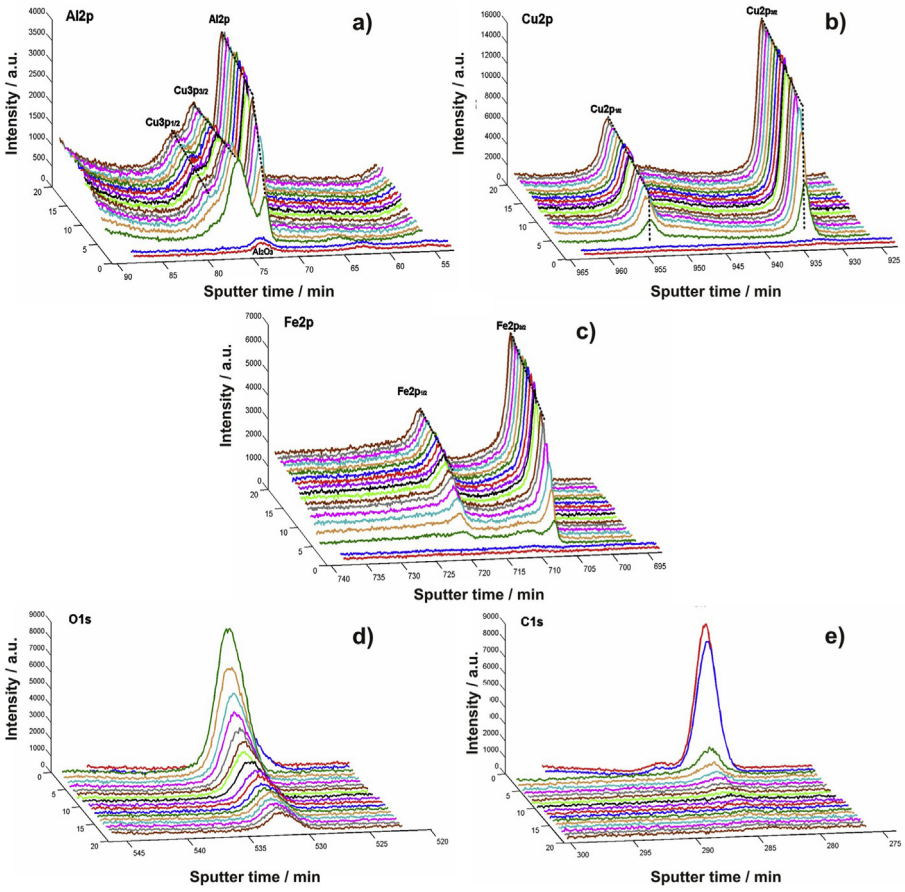

Fig. 7. XPS narrow scan spectra of Al2p (a), Cu2p (b), Fe2p (c), O1s (d) and C1s (e) of $Al_{65}Cu_{20}Fe_{15}$ plate after corrosion test in 3.5% NaCl solution at 25 °C.

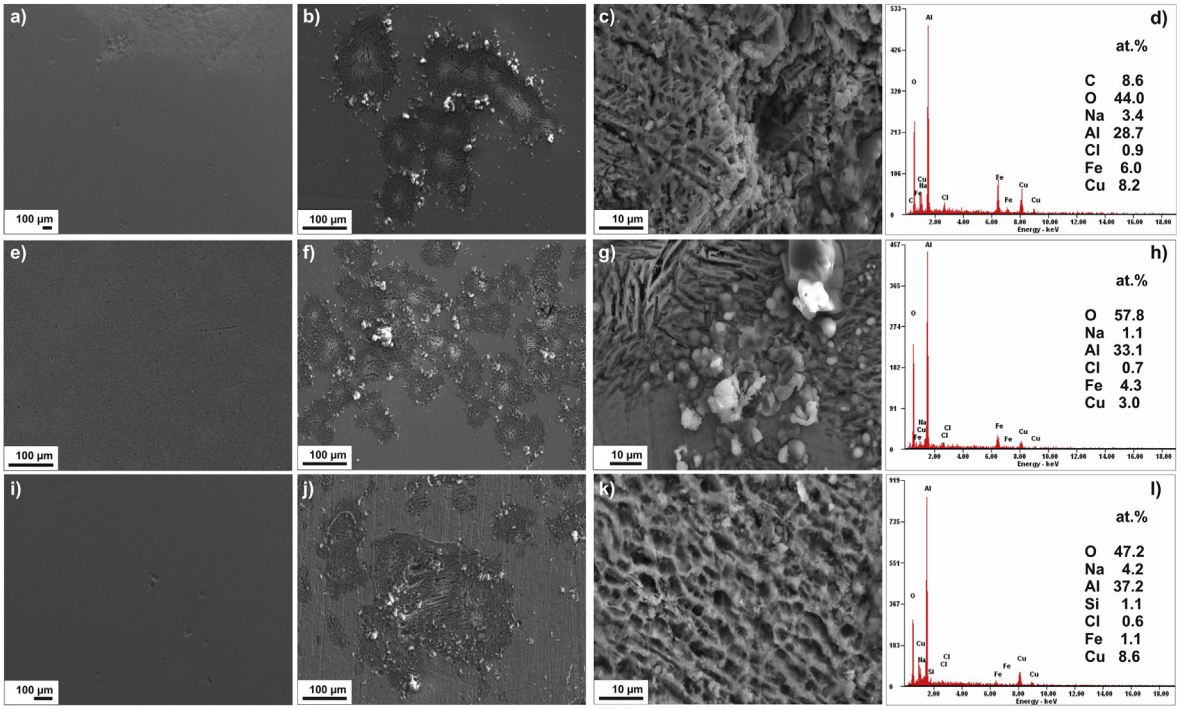

Fig. 8. SEM micrographs (a-c, e-g, i-k) and EDS (d,h,l) analysis of the surface morphology of $Al_{65}Cu_{20}Fe_{15}$, $Al_{78}Cu_7Fe_{15}$, and $Al_{80}Cu_5Fe_{14}Si_1$ plate after electrochemical tests in 3.5% NaCl solution at 25 °C.

Table 3
Hardness values of the $Al_{65}Cu_{20}Fe_{15}$, $Al_{78}Cu_7Fe_{15}$ and $Al_{80}Cu_5Fe_{14}Si_1$ alloys in the form of plates.

No.	$Al_{65}Cu_{20}Fe_{15}$	$Al_{78}Cu_7Fe_{15}$	$Al_{80}Cu_5Fe_{14}Si_1$
1	924	496	308
2	807	483	411
3	884	478	440
4	900	513	595
5	859	504	555
6	909	492	497
7	824	502	509
8	884	509	461
9	823	488	400
10	888	485	500
Average	870 HV	495 HV	468 HV

5. Conclusions

1 The preparation method (master alloy melting and plate casting) influences the formation of quasicrystalline and intermetallic phases in Al–Cu–Fe alloys, and process of plate casting results in a decrease of the crystal size.
2 The corrosion resistance tests of the tested alloys has been conducted in 3.5% NaCl solution at 298 K, and the results show that the highest corrosion resistance has been observed for the $Al_{65}Cu_{20}Fe_{15}$ alloy and the lowest resistance for the $Al_{78}Cu_7Fe_{15}$ alloy. Moreover, the better corrosion resistance parameters are noted for the samples formed by plate casting, rather than those in the master alloy state.
3 The SEM observations confirm the presence of corrosion centers in which porous structures occur. The hardness values of $Al_{78}Cu_7Fe_{15}$ and $Al_{80}Cu_5Fe_{14}Si_1$ plates are similar. The hardness of the $Al_{65}Cu_{20}Fe_{15}$ alloy is significantly higher than the other two alloys.

Declaration of competing interest

The authors declare that they have no known competing financial interests or personal relationships that could have appeared to influence the work reported in this paper.

Acknowledgments

The work was supported by the National Science Centre, Poland under research project no.: 2018/29/B/ST8/02264.

References

[1] B. Markoli, T. Bončina, F. Zupanič, Mater. Werkst. 43 (2012) 340–344.
[2] A. Školáková, P. Novák, L. Mejzlíková, F. Pruša, P. Salvetr, D. Vojtěch, Materials 10 (2017) 2–19.
[3] F. Zupanič, C. Gspan, T. Bončina, Light Met. (2016) 255–258.
[4] F. Schurack, J. Eckert, L. Schultz, Acta Mater. 49 (2001) 1351–1361.
[5] M. Gogebakan, B. Avar, M. Tarakci, J. All. Compd. 509S (2011) 316–319.
[6] M. Roy, JMMM 302 (2006) 52–55.
[7] E. Huttunen-Saarivirta, J. Vuorinen, Intermetallics 13 (2005) 885–895.
[8] P. Novák, A. Michalcová, M. Voděrová, I. Marek, D. Vojtěch, Mater. Eng. 20 (2013) 77–82.
[9] A.I. Salimon, A.P. Shevchukov, A.A. Stepashkin, V.V. Tcherdyntsev, L.K. Olifirov, S.D. Kaloshkin, J. All. Compd. 707 (2017) 315–320.
[10] W. Wolf, F.G. Coury, M.J. Kaufman, C. Bolfarini, C.S. Kiminami, W.J. Botta, J. All. Compd. 731 (2018) 1288–1294.
[11] M. Göğebakan, B. Avar, O. Uzun, Mater. Sci. 27 (2009) 919–926.
[12] Y.V. Mil'man, N.A. Efimov, S.V. Ul'shin, A.I. Bykov, O.D. Neikov, A.V. Samelyuk, Powder Metall. Met Ceram. 49 (2010) 280–288.
[13] H. Parsamehr, S.Y. Chang, C.H. Lai, J. All. Compd. 732 (2018) 952–957.
[14] M.A. Suárez, R. Esquivel, J. Alcántara, H. Dorantes, J.F. Chávez, Mater. Char. 62 (2011) 917–923.
[15] E. Huttunen-Saarivirta, J. All. Compd. 363 (2004) 150–174.
[16] K. Lee, J. Hsu, D. Naugle, H. Liang, Mater. Des. 108 (2016) 440–447.
[17] L. Lityńska-Dobrzyńska, M. Mitka, A. Góral, K. Stan-Głowińska, J. Dutkiewicz, Mater. Char. 117 (2016) 127–133.
[18] C. Li, C. Carey, D. Li, M. Caputo, R. Bouch, H. Hampikian, Mater. Char. 140 (2018) 162–171.
[19] L. Lityńska-Dobrzyńska, J. Dutkiewicz, K. Stan-Głowińska, L. Dembinski, C. Coddet, P. Ochin, Acta Phys. Pol., A 126 (2014) 512–515.
[20] C. Li, C. Carey, D. Li, M. Caputo, H. Hampikian, Microsc. Microanal. 24 (2018) 1032–1033.
[21] S.M. Lee, B.H. Kim, S.H. Kim, E. Fleury, W.T. Kim, D.H. Kim, Mater. Sci. Eng., A 294–296 (2000) 93–98.
[22] J. Zhang, Y. Xue, Y. Guo, C. Xu, W. Liang, Mater. Sci. Forum 546–549 (2007) 619–622.
[23] A. Prekul, N. Shchegolikhina, Crystals 6 (2016) 119.
[24] E.V. Shalaeva, A.F. Prekul, N.I. Shchegolikhina, N.I. Medvedeva, Acta Phys. Pol., A 126 (2014) 572–576.
[25] J. Teillet, B. Bouchet-Fabre, Hyperfine Interact. 55 (1990) 1077–1082.
[26] L.C.L.A. Jamshidi, R.J. Rodbari, L. Nascimento, C.M.B.M. Barbosa, Rev. Cubana Quím. 29/1 (2017) 150–166.
[27] L.C.L.A. Jamshidi, R.J. Rodbari, Evolution of the phases of quasicrystalline alloys icosahedral/decagonal $Al_{62.2}Cu_{25.3}Fe_{12.5}$/$Al_{65}Ni_{15}Co_{20}$ and oxidative behavior, J. Chil. Chem. Soc. 63/2 (2018) 3928–3933.
[28] Y. Massiani, S.A. Yaazza, J.P. Crousier, J.M. Dubois, J. Non-Cryst. Solids 159 (1993) 92–100.
[29] A. Rüdiger, U. Köster, Mater. Sci. Eng. 294–296 (2000) 890–893.
[30] E. Huttunen-Saarivirta, T. Tiainen, Mater. Chem. Phys. 85 (2004) 383–395.
[31] E.V. Sukhovaya, V. Polonskyy, Y. Ustinova, M.V. Berun, Metal Sci. Treat. Metals 4 (2018) 19–26.
[32] S.I. Ryabtsev, O.V. Sukhova, V.A. Polonskyy, J. Phys. Electron. 27/1 (2019) 27–30.
[33] O.V. Sukhova, V.A. Polonskyy, K.V. Ustinova, Mater. Sci. 55 (2019) 138–145.
[34] N.H. Pryds, X. Huang, Metall. Mater. Trans. A Phys. Metall. Mater. Sci. 31 (2000) 3155–3166.
[35] E. McCafferty, Corrosion Sci. 47 (2005) 3202–3215.
[36] Y. Calvayrac, A. Quivy, M. Bessiere, S. Lefebvre, M. Cornier-Quiquandon, D. Gratias, J. Phys. France 51 (1990) 417–431.
[37] S.D. Ponja, I.P. Parkin, C.J. Carmalt, RSC Adv. 6 (2016) 102956–102960.
[38] E.V. Sukhovaya, V. Polonskyy, Y. Ustinova, Metallofiz. Nov. Tekh. 40 (2018) 1475–1487.